Stepsize sharing in time-lapse full-waveform inversion

Xin Fu and Kris Innanen

ABSTRACT

Full waveform inversion (FWI) methods can produce high-resolution images of the physical properties of the subsurface. It has become a powerful tool for time-lapse or 4D seismic inversion, with applications in the monitoring of reservoir changes with injection and production, and potentially long term storage of carbon. Current time-lapse FWI strategies include the parallel strategy (PRS), the sequential strategy (SQS), the double-difference strategy (DDS), the common-model strategy (CMS), and the central-difference strategy (CDS). PRS time-lapse inversion is affected by convergence differences between the baseline and monitoring inversions, as well as non-repeatable noise and non-repeatable acquisition geometries between surveys. The other strategies above are largely efforts to fix these sensitivities of PRS. In this paper, we introduce and examine two strategies, which we refer to as stepsize-sharing PRS (SSPRS) and stepsize-sharing CMS (SSCMS). As the name suggests, they are characterized by a sharing of update stepsizes between baseline and monitoring stages of the time-lapse FWI. Synthetic data tests indicate that stepsize-sharing reduces artifacts caused by the PRS convergence variability. In particular, the stepsize-sharing common-model strategy (SSCMS) appears to be adept at reducing artifacts caused by all of convergence differences, non-repeated noise, non-repeatable source locations, and biased starting models. This breadth of robustness does not appear in any of the other approaches tested. Especially given that SSCMS through its sharing incurs half of the computational cost of CMS and CDS, we regard the workflow as being worth further study.

INTRODUCTION

Time-lapse or 4D seismic analysis is a crucial technology for reservoir monitoring problems such as enhanced oil recovery and CO_2 storage (Greaves and Fulp, 1987; Ross and Altan, 1997; Wang et al., 1998; Barkved et al., 2003; Arts et al., 2003; Barkved et al., 2005; Chadwick et al., 2009; Kazemeini et al., 2010; Pevzner et al., 2017). It has begun to be incorporated as a matter of course into reservoir development plans (Jack, 2017). In non time-lapse seismic problems, static geological information and that of dynamic fluid flow and processes underoing change are interweaved, whereas, in the time-lapse seismic problem static information can be suppressed to emphasize dynamic, time-variant processes (Lumley, 2001).

Full waveform inversion (FWI) (Lailly et al., 1983; Tarantola, 1984; Virieux and Operto, 2009), a technology with the capacity to create high-resolution images of physical properties of subsurface media, has become a powerful tool for time-lapse inversion. Real field data applications have been reported with increased frequency recently (Raknes and Arntsen, 2014; Hicks et al., 2016; Yang et al., 2016; Kamei et al., 2017; Fabien-Ouellet et al., 2017; Bortoni et al., 2021), but challenges remain quite significant. The time-lapse FWI approach mostly likely to be currently considered "conventional" is known as the parallel strategy (PRS). In PRS, baseline and monitor inversions are carried out independently

but using the same starting model. Its challenges derive from detailed differences within the the two independent inversions within it. They commonly exhibit different convergence properties, and these induce artifacts in the time-lapse inversion. Furthermore, as we will demonstrate in this paper, it is sensitive to non-repeatable random noise. To avoid some of these issues, Routh et al. (2012) introduced sequential strategy (SQS), which uses the inverted baseline as the starting model for the monitor inversion. However, examples presented by Yang et al. (2015) and Zhou and Lumley (2021a) indicate that it can cause strong artifacts in the time-lapse inversion by amplifying convergence differences between the baseline and monitor inversions. Target-oriented SQS (Raknes and Arntsen, 2014; Asnaashari et al., 2015) has been shown to effectively constrain artifacts in the target zone, this mitigation strategy requires significant prior information, especially about the location of time-lapse change. Probably the most widely-adopted strategy at the moment is the double-difference strategy (DDS), proposed by Zheng et al. (2011), which has been used and adapted by many researchers (Zhang and Huang, 2013; Raknes et al., 2013; Fu and Innanen, 2021), and has been vetted with real data case in Yang et al. (2016). It has several points of weakness, some of which are addressable. For instance, Fu et al. (2020) introduced a double-wavelet DDS to mitigate the impact of non-repeatability of baseline and monitor source wavelets to the inversion. However, DDS remains very sensitive to non-repeatability of source/receiver locations (Yang et al., 2015; Zhou and Lumley, 2021b). A different approach was taken by Hicks et al. (2016), who introduced the common-model strategy (CMS) and applied it to a North Sea field case study; it was adopted by Bortoni et al. (2021) in real data of a post-salt field in the Campos Basin. A different variant, introduced by (Zhou and Lumley, 2021a) and called the central-difference strategy (CDS), has recently been shown to be robust to non-repeatable noise in time-lapse FWI (Zhou and Lumley, 2021b). As they are amongst the most recent and robust time-lapse methods in the literature, we will examine CMS and CDS under different conditions in this paper.

The main results of this paper are two new candidate time-lapse FWI strategies, which aim to grow and extend the robustnesses sought in the above references, and simultaneously address computational burden. The main concept we will leverage is the sharing of waveform inversion stepsizes across baseline and monitoring inversions. Conclusions are based on benchmark synthetic data and comparative inversions with the new and recent methods.

TIME-LAPSE FWI METHODS

In standard FWI (Lailly et al., 1983; Tarantola, 1984; Virieux and Operto, 2009) we minimize the L2 norm misfit function:

$$E(\mathbf{m}) = \frac{1}{2}||\mathbf{d}_{obs} - \mathbf{F}(\mathbf{m})||^2, \tag{1}$$

where $\mathbf{d}_{obs}$ is the observed data or recorded wavefields, $\mathbf{F}(\cdot)$ is a forward modeling operator based on the wave equation, and $\mathbf{m}$ is the updating model (e.g., P-wave velocity). Via some appropriate optimization approach, based on steepest descents, conjugate gradients, etc., the model is updated iteratively as:

$$\mathbf{m}^k = \mathbf{m}^{k-1} + \delta\mathbf{m}^k, \tag{2}$$

where k is the iteration number, and

$$\delta \mathbf{m}^k = \mu^k \mathbf{g}(\mathbf{m}^{k-1}, \mathbf{d}_{res}^{k-1}), \tag{3}$$

where

$$\mathbf{d}_{res}^{k-1} = \mathbf{d}_{obs} - \mathbf{F}(\mathbf{m}^{k-1}), \tag{4}$$

in which $\mathbf{g}(\mathbf{m}^{k-1}, \mathbf{d}_{res}^{k-1})$ is the updating direction of model in iteration k, which depends on the updated model $\mathbf{m}^{k-1}$ and data residual $\mathbf{d}_{res}^{k-1}$ in iteration $k-1$. In the steepest descent method, $\mathbf{g}$ represents the gradient of the misfit function (equation 1) with respect to $\mathbf{m}$, which is the zero-lag cross-correlation between forward wavefileds and backward wavefields of data residuals. For the first iteration, a starting model $\mathbf{m}^0$ have to be prepared, which can be obtained by velocity analysis or tomography. Furthermore, combining equation 3 and 4, we have

$$\delta \mathbf{m}^k = \mu^k \mathbf{g}(\mathbf{m}^{k-1}, \mathbf{d}_{obs}), \tag{5}$$

where the updating direction $\mathbf{g}$ depends on observed data and the updated model $\mathbf{m}^{k-1}$ in iteration $k-1$. In this study, we use a time-domain constant-density acoustic finite-difference method as the forward modeling operator, the steepest descent method as the optimization, and we precondition the gradient with the diagonal approximation of the Hessian matrix (Shin et al., 2001).

Common time-lapse inversion strategies

Parallel strategy

The parallel strategy (PRS) follows the workflow in Figure 1a. It includes two independent FWI processes: baseline model inversion, with baseline data and a starting model as inputs, and monitor model inversion, with monitor data and the same (baselind) starting model as inputs. The estimated time-lapse model is the difference between the inverted monitor model and the inverted baseline model. Since FWI is highly non-linear, with local minima as common traps, the two FWI processes mentioned above often have different convergence properties, with each difference tending to produce artifacts upon subtraction.

Sequential strategy

The sequential strategy (SQS) is summarized in the workflow in Figure 1b. It involves has the same baseline inversion as PRS, and takes baseline data and a starting model as input. The monitor inversion is different. In it, the inverted baseline model is used as the starting model for the monitor inversion, and the difference of the two final inversions is the time-lapse model. Inversions with different starting models also tend to produce different convergence histories, however, and again strong artifacts are the result (Yang et al., 2015; Fu et al., 2020; Zhou and Lumley, 2021a). We do not pursue SQS further in this study.

Double-difference strategy

The double-difference strategy (DDS), with workflow illustrated in Figure 1c, also contains two FWI steps. The first is again the baseline model inversion. In the second, the

starting model is the inverted baseline model, as with SQS, but the input monitor data are not the observed monitor data. Instead, a composited data set is introduced:

$$\mathbf{d}_{DD} = \mathbf{F}(\mathbf{m}_{bas}) + (\mathbf{d}_{mon} - \mathbf{d}_{bas}), \tag{6}$$

where $\mathbf{F}(\mathbf{m}_{bas})$ are synthetic data predicted from the inverted baseline model $\mathbf{m}_{bas}$, $(\mathbf{d}_{mon} - \mathbf{d}_{bas})$ are difference data (observed monitor data $\mathbf{d}_{mon}$ minus the observed baseline data $\mathbf{d}_{bas}$). Accordingly, the misfit function for the monitor inversion becomes:

$$\mathbf{E}_{DD}(\mathbf{m}_{mon}) = \frac{1}{2}||\mathbf{d}_{DD} - \mathbf{F}(\mathbf{m}_{mon})||^2, \tag{7}$$

where $\mathbf{F}(\mathbf{m}_{mon})$ are the synthetic data predicted from the inverted monitor model $\mathbf{m}_{mon}$. Rewriting equation 7 as:

$$\mathbf{E}_{DD}(\mathbf{m}_{mon}) = \frac{1}{2}||(\mathbf{d}_{mon} - \mathbf{F}(\mathbf{m}_{mon})) - (\mathbf{d}_{bas} - \mathbf{F}(\mathbf{m}_{bas}))||^2, \tag{8}$$

we observe that minimizing the misfit function tends to equalize the baseline data residual and the monitor data residual. DDS can reduce convergence differences between baseline and monitor inversions, tending to suppress artifacts outside of the time-lapse change zone. It is, in other words, a kind of target-oriented strategy. Its disadvantages arise largely in difference data in equation 6, which are often weak. The signal is easy influenced by non-repeatability in time-lapse surveys, and those differences can leak strongly into the time-lapse model.

Common-model strategy

The common-model strategy (CMS), with workflow illustrated in Figure 1d, can be seen as an upgraded version of the PRS. Essentially, it contains two instances of PRS. First, the baseline and monitor inversions are performed independently with the same starting model. Then a new starting model is taken from the average of the baseline and monitor models; with this, the baseline and monitor inversions are performed independently again, still with the original data sets. The final time-lapse model is obtained from a difference of the baseline and monitor models derived during the second PRS. Although essentially an upgraded PRS, the CMS strategy has proved in both synthetic and field case studies to outperform the PRS on account of the changes in the effective baseline model (Hicks et al., 2016).

Central-difference strategy

The central-difference strategy (CDS), with workflow illustrated in Figure 1e comprises two instances of SQS, called the forward bootstrap FWI and the reverse bootstrap FWI. The forward bootstrap FWI uses the baseline data and a starting model to invert for a baseline model; then it uses the inverted baseline model as the starting model for monitor inversion. The first time-lapse model is obtained by subtracting the baseline model from the monitor model, and the second (i.e., the reverse bootstrap FWI) uses the monitor data and the same starting model as in the first FWI to invert for the monitor model. Then the

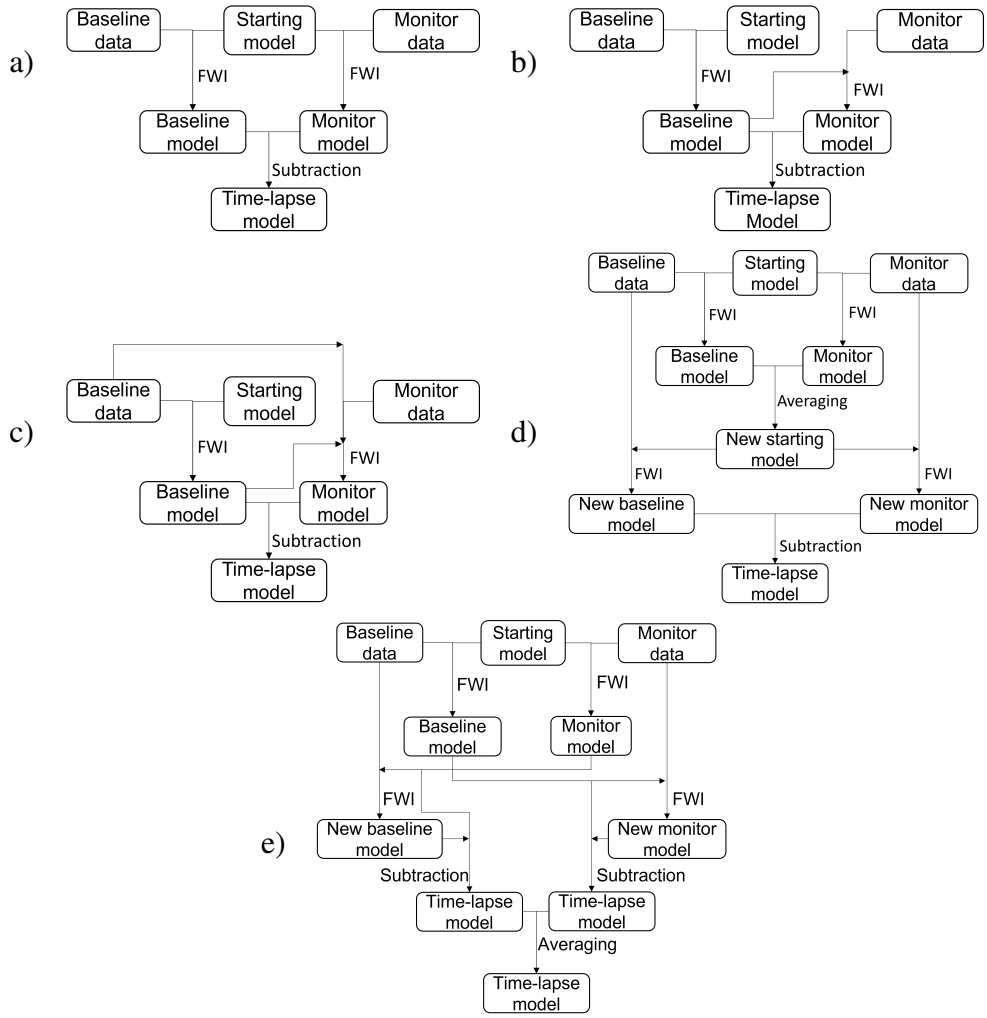

FIG. 1. Flowcharts of present time-lapse FWI strategies. (a) Parallel strategy (PRS). (b) Sequential strategy (SQS). (c) Double-difference strategy (DDS). (d) Common-model strategy (CMS). (e) Central-difference strategy (CDS).

inverted monitor model is used as the starting model for baseline model inversion. The second time-lapse model is obtained by subtracting the baseline model from the monitor model. The final time-lapse model is the average of these two time-lapse models. Zhou and Lumley (2021a) find that artifacts in the first and second time-lapse models have opposite phases, whereas the correct time-lapse estimations in the two models have identical phases, hence the artifacts are attenuated after averaging the two models.

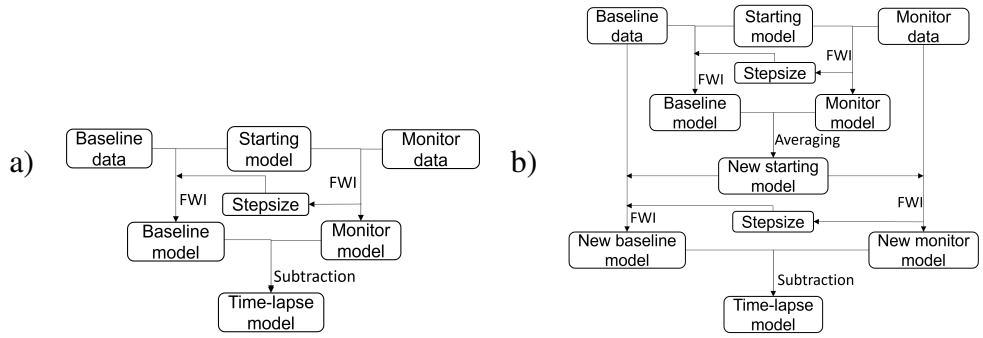

FIG. 2. Flowcharts of stepsizes-sharing time-lapse FWI strategies. (a) Stepsizes-sharing parallel strategy (SSPRS). (b) Stepsizes-sharing common-model strategy (SSCMS).

STEPSIZE SHARING TIME-LAPSE INVERSION STRATEGIES

In this section, we propose two new strategies for time-lapse FWI that add to these mitigating efforts the idea of sharing of stepsizes. Returning to the sequence in equations 2 to 5, if we substituted equation 5 into 2, we produce an expression for an updated baseline model at iteration k:

$$\mathbf{m}_{bas}^{k} = \mathbf{m}_{bas}^{k-1} + \mu_{bas}^{k}\mathbf{g}(\mathbf{m}_{bas}^{k-1}, \mathbf{d}_{bas,obs}), \tag{9}$$

and an updated monitor model at iteration k expressed as:

$$\mathbf{m}_{mon}^{k} = \mathbf{m}_{mon}^{k-1} + \mu_{mon}^{k}\mathbf{g}(\mathbf{m}_{mon}^{k-1}, \mathbf{d}_{mon,obs}). \tag{10}$$

At the end of two FWI procedures, the inverted baseline and monitor models are, respectively:

$$\mathbf{m}_{bas} = \mathbf{m}_{bas}^{0} + \sum_{k=1}^{m} \mu_{bas}^{k}\mathbf{g}(\mathbf{m}_{bas}^{k-1}, \mathbf{d}_{bas,obs}), \tag{11}$$

and

$$\mathbf{m}_{mon} = \mathbf{m}_{mon}^{0} + \sum_{k=1}^{n} \mu_{mon}^{k}\mathbf{g}(\mathbf{m}_{mon}^{k-1}, \mathbf{d}_{mon,obs}), \tag{12}$$

where $\mathbf{m}_{bas}^{0}$ and $\mathbf{m}_{mon}^{0}$ are, respectively, the starting models for baseline and monitor inversions, and m and n are the maximum baseline and monitor iteration numbers, respectively. Let

$$\mathbf{d}_{dif} = \mathbf{d}_{mon,obs} - \mathbf{d}_{bas,obs},$$

be the difference data, and

$$\mathbf{m}_{mon}^{k-1} = \mathbf{m}_{mon,bas}^{k-1} + \mathbf{m}_{tl}^{k-1},$$

in which $\mathbf{m}_{mon,bas}^{k-1}$ is the baseline model implied by the monitor model $\mathbf{m}_{mon}^{k-1}$ and $\mathbf{m}_{tl}^{k-1}$ is the time-lapse model in iteration $k-1$. With these in place we have

$$\mathbf{m}_{mon} = \mathbf{m}_{mon}^{0} + \sum_{k=1}^{n} \mu_{mon}^{k}\mathbf{g}(\mathbf{m}_{mon,bas}^{k-1} + \mathbf{m}_{tl}^{k-1}, \mathbf{d}_{bas,obs} + \mathbf{d}_{dif}). \tag{13}$$

Since $\mathbf{g}$ is linear with respect to the observed data, equation 13 can be rewritten as:

$$\mathbf{m}_{mon} = \mathbf{m}^0_{mon} + \sum_{k=1}^{n} \mu^k_{mon} \mathbf{g}(\mathbf{m}^{k-1}_{mon,bas} + \mathbf{m}^{k-1}_{tl}, \mathbf{d}_{bas,obs}) + \sum_{k=1}^{n} \mu^k_{mon} \mathbf{g}(\mathbf{m}^{k-1}_{mon,bas} + \mathbf{m}^{k-1}_{tl}, \mathbf{d}_{dif}). \tag{14}$$

The quantity $\mathbf{g}$ is nonlinear with respect to the model, so we approximate the updating direction by Taylor expansion as:

$$\mathbf{g}(\mathbf{m}^{k-1}_{mon,bas} + \mathbf{m}^{k-1}_{tl}, \mathbf{d}_{bas,obs}) \approx \mathbf{g}(\mathbf{m}^{k-1}_{mon,bas}, \mathbf{d}_{bas,obs}) + \mathbf{g}^{'}(\mathbf{m}^{k-1}_{mon,bas}, \mathbf{d}_{bas,obs}) \mathbf{m}^{k-1}_{tl}, \tag{15}$$

where $\mathbf{g}^{'}$ is the derivative of the updating direction $\mathbf{g}$ with respect to model $\mathbf{m}^{k-1}_{mon,bas}$. Putting equation 15 into equation 14, we have

$$\begin{aligned} \mathbf{m}_{mon} = \mathbf{m}^0_{mon} &+ \sum_{k=1}^{n} \mu^k_{mon} \mathbf{g}(\mathbf{m}^{k-1}_{mon,bas}, \mathbf{d}_{bas,obs}) + \sum_{k=1}^{n} \mu^k_{mon} \mathbf{g}^{'}(\mathbf{m}^{k-1}_{mon,bas}, \mathbf{d}_{bas,obs}) \mathbf{m}^{k-1}_{tl} \\ &+ \sum_{k=1}^{n} \mu^k_{mon} \mathbf{g}(\mathbf{m}^{k-1}_{mon}, \mathbf{d}_{dif}). \end{aligned} \tag{16}$$

or

$$\mathbf{m}_{mon} = \mathbf{m}_{mon,bas} + \mathbf{m}_{tl}, \tag{17}$$

where

$$\mathbf{m}_{mon,bas} = \mathbf{m}^0_{mon} + \sum_{k=1}^{n} \mu^k_{mon} \mathbf{g}(\mathbf{m}^{k-1}_{mon,bas}, \mathbf{d}_{bas,obs}), \tag{18}$$

$$\mathbf{m}_{tl} = \sum_{k=1}^{n} \mu^k_{mon} \mathbf{g}^{'}(\mathbf{m}_{mon,bas}, \mathbf{d}_{bas,obs}) \mathbf{m}^{k-1}_{tl} + \sum_{k=1}^{n} \mu^k_{mon} \mathbf{g}(\mathbf{m}^{k-1}_{mon}, \mathbf{d}_{dif}). \tag{19}$$

Comparing equation 11 with equation 18, we observe that the implicit baseline model can be eliminated from the inverted monitor model under the conditions:

(1) We employ the same starting model, i.e. $\mathbf{m}^0_{bas} = \mathbf{m}^0_{mon}$;

(2) The iteration number is the same, i.e. $m = n$;

(3) The stepsizes are the same, i.e. $\mu^k_{mon} = \mu^k_{bas}$;

(4) The updated baseline models are the same, i.e. $\mathbf{m}^{k-1}_{mon,bas} = \mathbf{m}^{k-1}_{bas}$.

Conditions (1) and (3) in fact enforce condition (4), since equations 11 and 18 are recursive. Hence, we only need to meet the first three conditions to eliminate the implicit baseline model.

In PRS, two FWI procedures are enacted, starting from the same model, $\mathbf{m}^0_{bas} = \mathbf{m}^0_{mon}$, and having the same iteration number, $m = n$ (the case of different iteration numbers normally enhances artifacts on the final time-lapse model). The implicit baseline model

$\mathbf{m}_{mon,bas}$ cannot be eliminated completely in the PRS, since the condition (3) is not met. The remaining baseline model can be considered the source of the coherent artifacts in the final time-lapse model.

PRS can be adapted to produce the stepsize-sharing parallel strategy (SSPRS), to meet the condition (3), wherein $\mu^k_{mon} = \mu^k_{bas}$, such that the implicit baseline model is eliminated. The workflow is illustrated in Figure 2a, in which we perform the monitor inversion first with the inputs of a starting model and observed monitor data, and the outputs are not only the monitor model but also the stepsizes for each iteration. Then, in the second FWI, the baseline inversion, the inputs are not only the observed baseline data and the same starting model, but also the stepsizes from the first monitor inversion. The final time-lapse model is obtained by subtracting the baseline model from the monitor model. In addition to the elimination of what is largely a source of artifacts, an advantage of this SSPRS approach is that it saves on the cost of seeking the stepsizes during the second FWI. This is the first of the two proposed methods.

The CMS approach can also be upgraded to incorporate this idea, leading to the stepsize-sharing common-model strategy (SSCMS), the second of the two proposed methods. The workflow is illustrated in Figure 2b. It involves four FWI steps. The first two are the same as in SSPRS. In the second two, we repeat SSPRS but with a starting model comprising the average of the inverted baseline and monitor model in the first two. The final time-lapse model is the difference between the inverted monitor and baseline models in the second two FWI outputs.

The baseline updating directions ($\mathbf{g}(\mathbf{m}^{k-1}_{bas}, \mathbf{d}_{bas,obs})$) and the monitor updating directions ($\mathbf{g}(\mathbf{m}^{k-1}_{mon}, \mathbf{d}_{mon,obs})$) may not be produced at same scale, depending on the character of data noise and differences in baseline and monitor source/receiver locations. So, in both SSPRS and SSCMS, we recommend that the baseline and monitoring update directions be calibrated to a common root-mean-square before multiplying the shared stepsizes from monitor FWI.

NUMERICAL EXAMPLES

In this section, we use a land model to test our methods and have comparisons with present methods. The true baseline model is displayed in Figure 3a, two reservoirs are located at the left below corner and near the center, respectively. To mimic the fluid change, 4% or $49m/s$ velocity changes, displayed in Figure 3b, are added at the two reservoirs to obtain the monitor model. A smooth starting model is displayed in Figure 3c, which is employed in the first FWI of all time-lapse strategies mentioned above. The model size is 101-by-208 with 10m spacing. On the top of the model, seven sources are evenly spread at the depth of 10m and each surface cell grid is located a receiver. The source wavelet used for baseline and monitor data sets is identical, which is a minimum phase wavelet with a dominant frequency of $10Hz$. The time sampling interval is 2 milliseconds and the maximum recording time is 1.2 seconds. To show the capacity of the FWI program, a time-domain constant-density acoustic FWI, used in this study, we display the inverted baseline model in Figure 4a, and two traces crossing the two reservoirs at distances of 970m and 1700m are abstracted and plotted in Figure 4b. The results show a good performance

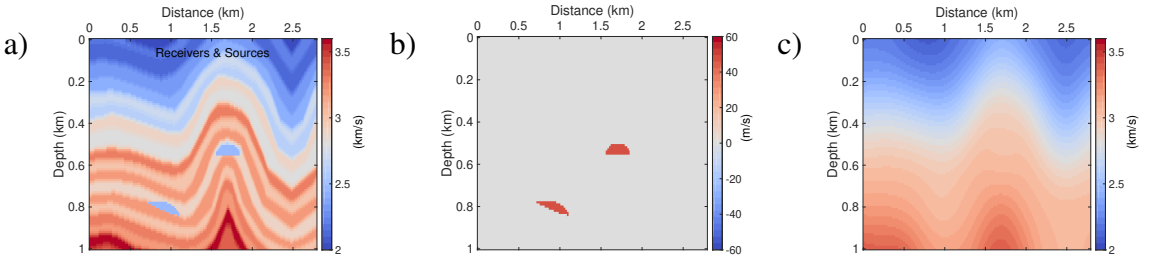

FIG. 3. (a) True baseline model and acquisition geometry. (b) True time-lapse model, all non-zero values are identical, $49m/s$, and clipped in $[-60, 60]$. (c) Starting model.

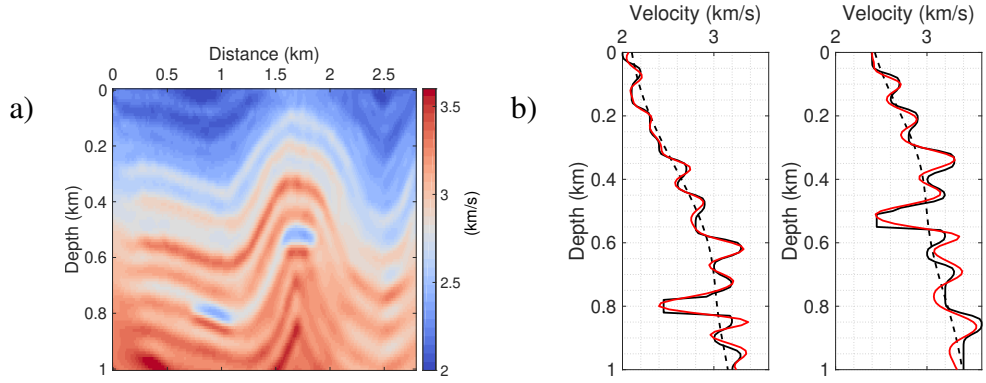

FIG. 4. (a) Inverted baseline model. (b) The solid black lines are the true model, the dash black lines are starting models, and the red lines are inverted baseline models at distance 970m (left) and 1700m (right).

of the FWI program. In the next subsections, we will implement the PRS, SSPRS, DDS, CMS, CDS, and SSCMS with noise-free data sets, noisy data sets, data sets with non-repeatable source locations, and biased starting models, and have comparisons between different strategies. All data sets are acoustic and synthetic, and all inversions have the same iteration number.

Noise-free data tests

In this subsection, noise-free data sets with perfectly repeatable acquisition geometries are employed. The result of different strategies are displayed in Figure 5, and the corresponding model errors (L1 norms of model residuals) are displayed in Figure 6. We observe the SSCMS gives the best result, and the DDS is slightly worse, which is followed by the SSPRS and CDS, and the worst results are given by the PRS and CMS. Comparing Figure 5a and b or Figure 5d and f, we observe sharing stepsizes between baseline and monitor inversions do help to reduce the artifacts caused by the convergence difference. Furthermore, the CMS cannot help to reduce the artifacts in the PRS, conversely, it enhances the artifacts. Overall, the SSPRS, DDS, CDS, and SSCMS all can help to reduce the artifacts in the PRS.

Non-repeatable random noise

In this subsection, noisy data sets with a perfectly repeatable acquisition geometry are employed. The noise added to the noise-free data is Gaussian random noise, and the noise

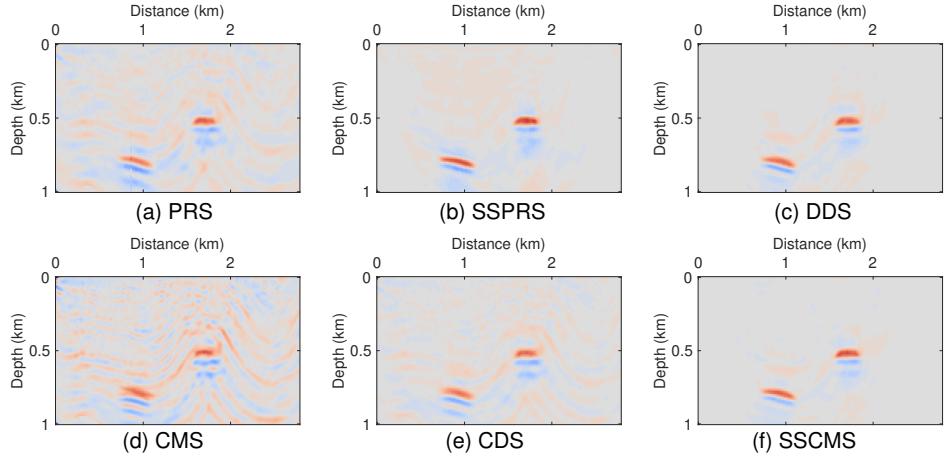

FIG. 5. Inverted time-lapse results using noise-free data for different strategies: (a) parallel strategy (PRS), (b) stepsize-sharing parallel strategy (SSPRS), (c) double-difference strategy (DDS), (d) common-model strategy (CMS), (e) central-difference strategy (CDS), (f) stepsize-sharing common-model strategy (SSCMS). All figures are clipped in the same color bar that in Figure 3b.

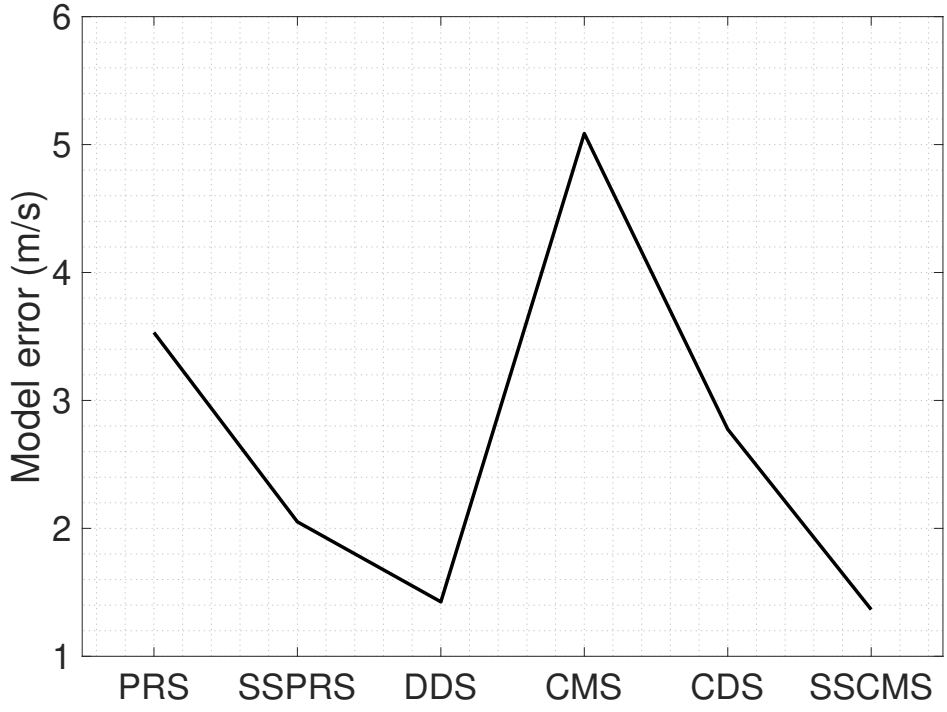

FIG. 6. Model errors of time-lapse results in Figure 5.

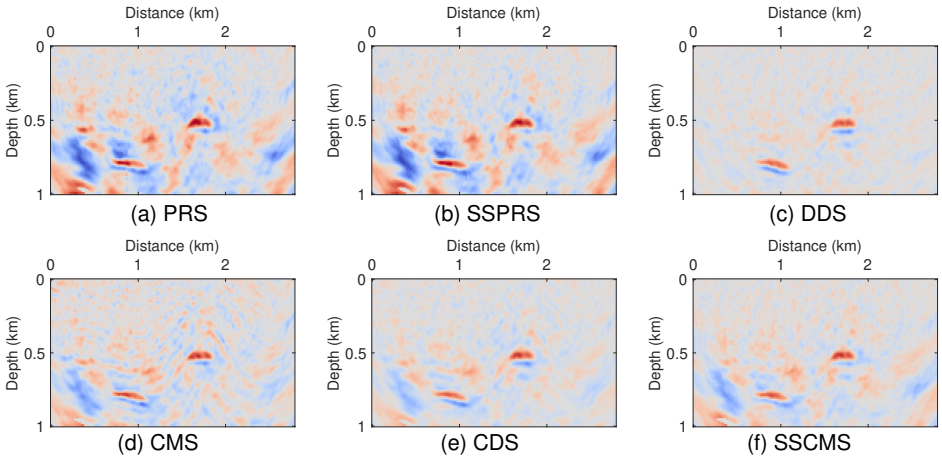

FIG. 7. Inverted time-lapse results using data with SNR=20 for different strategies. All figures are clipped in the same color bar that in Figure 3b.

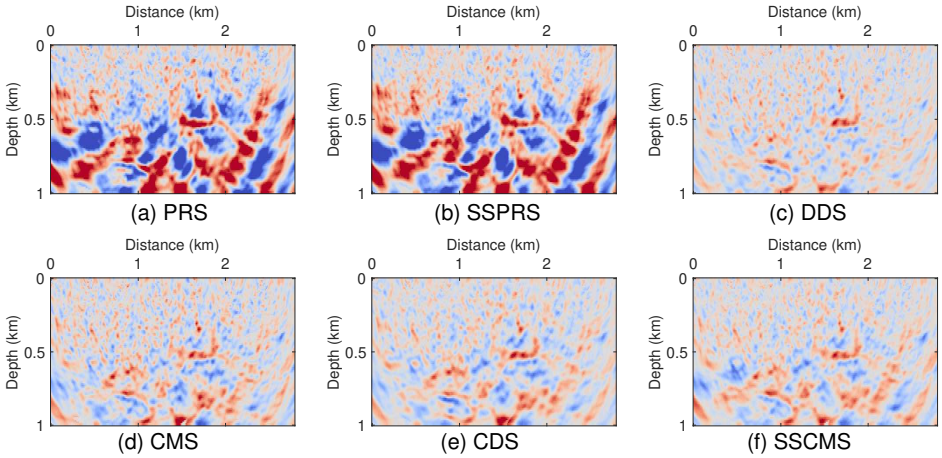

FIG. 8. Inverted time-lapse results using data with SNR=10 for different strategies. All figures are clipped in the same color bar that in Figure 3b.

level for baseline and monitor data is the same but from different implements. In Figure 7-9, we display the results of different strategies using data sets with SNR (signal-to-noise ratio) 20, 10, and 5. And the model errors of all results are plotted in Figure 10. We observe Comparing with the PRS and SSPRS, the other four strategies show a much better anti-noise property. Also, we observe the CMS, CDS, and SSCMS have similar performance, and the DDS is slightly better.

Non-repeatable source positions

In this subsection, noise-free data sets are used, but the acquisition geometries for baseline and monitor surveys are different. Normally, we have two cases in practice, the first is an acquisition geometry with sparse sources but dense receivers, the second is that with dense sources but sparse receivers. According to the reciprocal manner, the second case can be converted to the first to reduce the number forward modeling. So we only discuss the first case in our study. Moreover, the positioning non-repeatability can happen in sources or/and receivers. But for the case of dense receivers, we can uniform the receiver

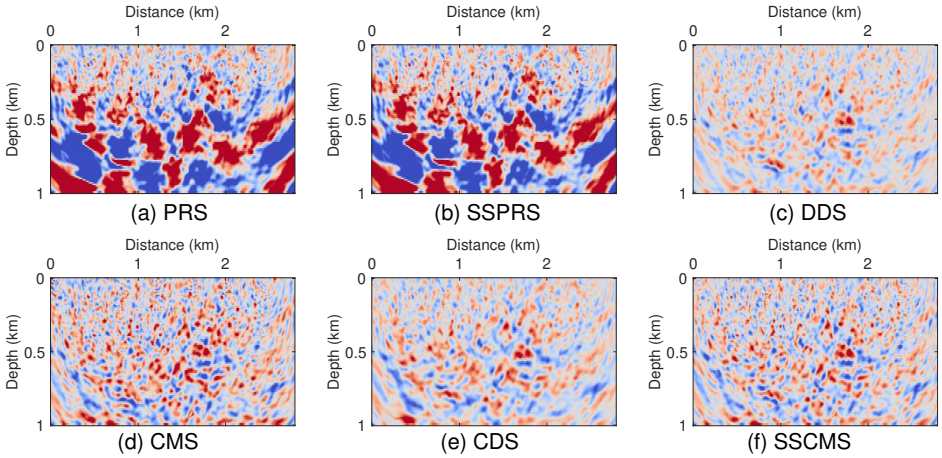

FIG. 9. Inverted time-lapse results using data with SNR=5 for different strategies. All figures are clipped in the same color bar that in Figure 3b.

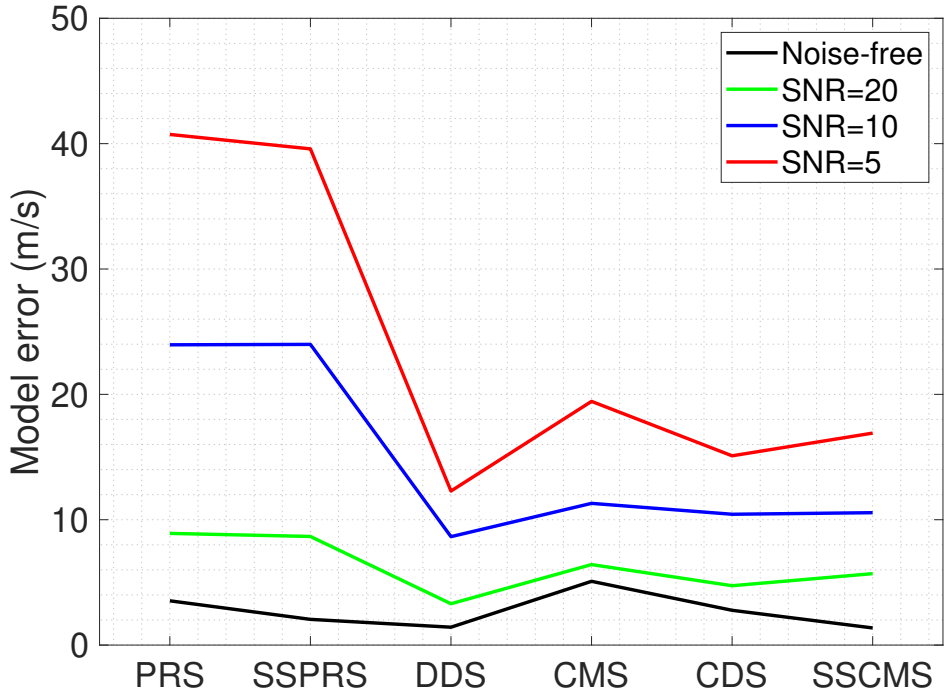

FIG. 10. Model errors of time-lapse results in Figure 5, 6, 7 and 8.

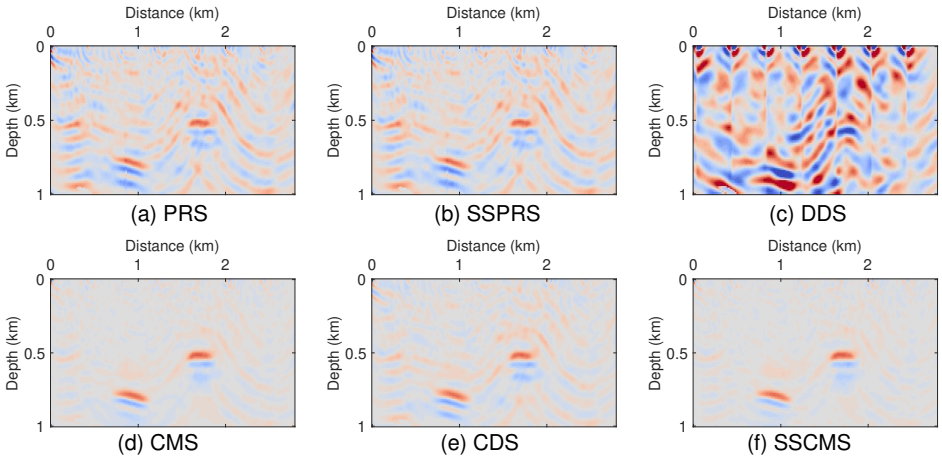

FIG. 11. Inverted time-lapse results of different strategies in the case of monitor source locations are 10m larger than baseline source locations. All figures are clipped in the same color bar that in Figure 3b.

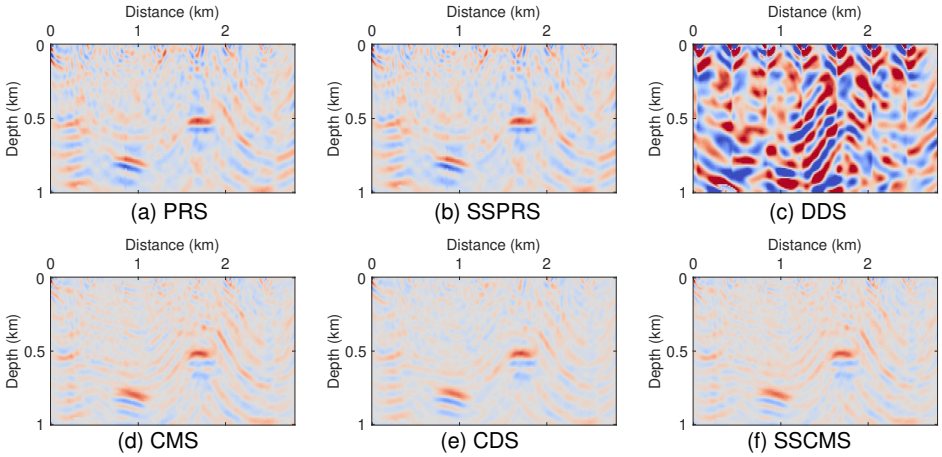

FIG. 12. Inverted time-lapse results of different strategies in the case of monitor source locations are 20m larger than baseline source locations. All figures are clipped in the same color bar that in Figure 3b.

positions by interpolation. Hence, in this study, we only investigate the effects of source positioning non-repeatability to time-lapse inversion strategies. The receiver is located in each surface cell grid of the model, and the seven monitoring source positions will move the same distance to the right from the baseline source position.

In Figure through 11 to 13, we plot the time-lapse results of different strategies and the source position differences between twice surveys are, respectively, 10m, 20, and 40m. And the corresponding model errors are plotted in Figure 14. We observe that the DDS is sensitive to the source position non-repeatability. The CMS, CDS, and SSCMS have similar results and are better than the PRS and SSPRS which are also similar.

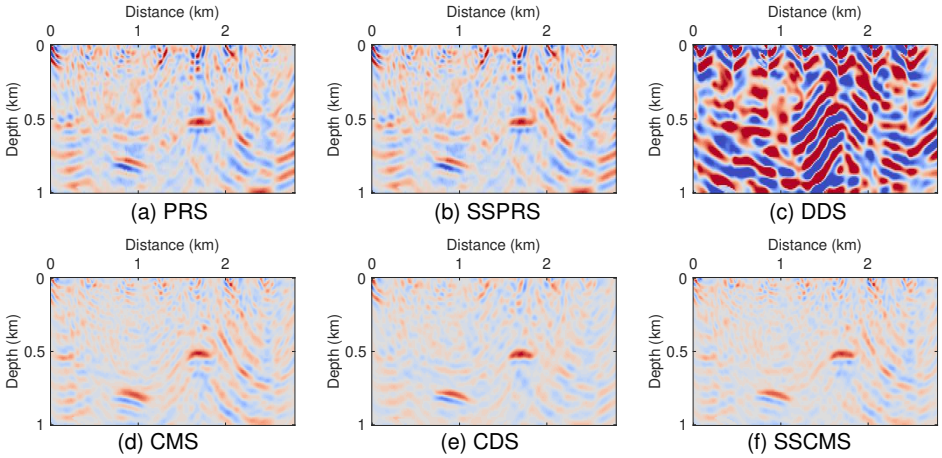

FIG. 13. Inverted time-lapse results of different strategies in the case of monitor source locations are 40m larger than baseline source locations. All figures are clipped in the same color bar that in Figure 3b.

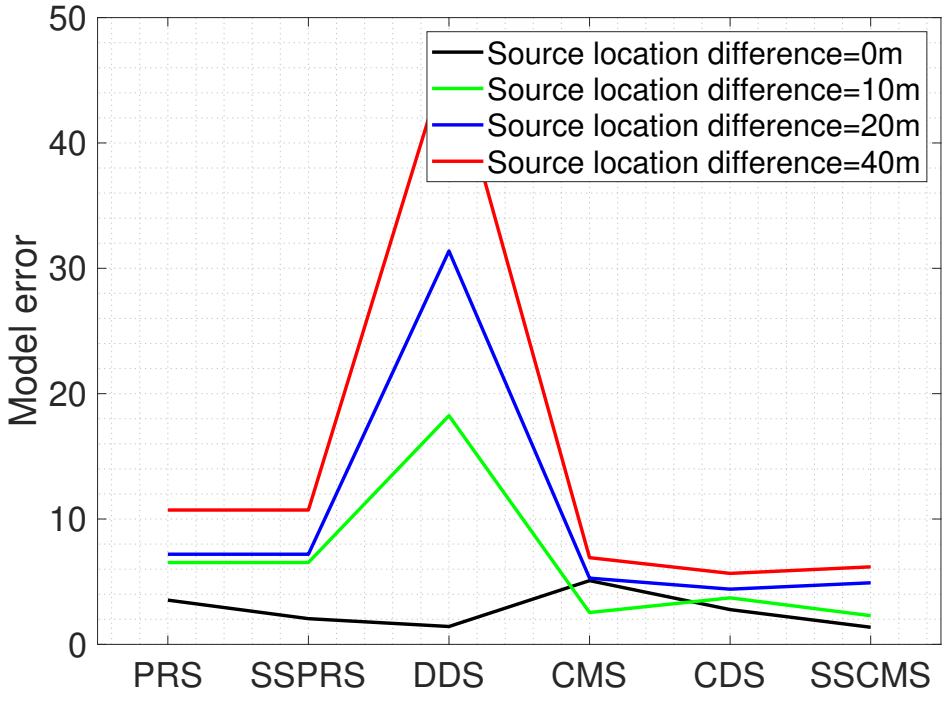

FIG. 14. Model errors of time-lapse results in Figure 5, 11, 12 and 13.

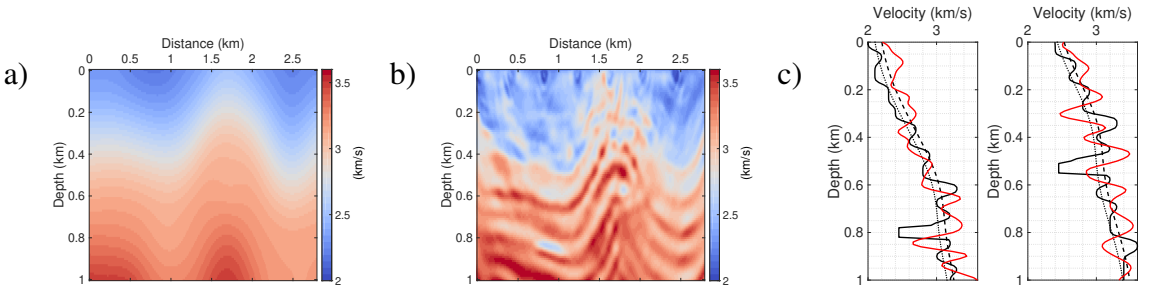

FIG. 15. (a) is the biased starting model which equals the unbiased model (Figure 3b) plus $100m/s$, and (b) is the corresponding inverted baseline model. (c) Traces abstracted at distances 970m (left) and 1700m (right), the solid black lines are the true model, the dash black lines are the biased starting models, the dot black lines are the unbiased starting models, and the red lines are inverted baseline models.

Biased starting models

In the previous tests, the starting model (Figure 3c) used is smoothed directly from the true baseline model (Figure 3a), which is an unbiased starting model crossing the center of the true model. In this subsection, we employ two biased starting models (Figure 15a and 16a) to test the different strategies with baseline and monitor data sets that are noise-free and are of identical acquisition geometries. The biased starting model in Figure 15a equals the unbiased model (Figure 3b) plus $100m/s$, and its corresponding inverted baseline model are plotted in Figure 15b and c. Another biased starting model plotted in Figure 15a equals the unbiased model minus $100m/s$, and its corresponding inverted baseline model is plotted in Figure 16b and c. In Figure 17a-c, the observed baseline data and the synthetic data of the inverted baseline models are plotted. From the figures, we observe that the biased starting models generate inversion results with serious deviations, but it can still clearly show the main geological structure, and all the deviated results have good data fitting. Since FWI is apt to plunge into a local minimum, and its result depends too much on starting model. The cases of biased starting models are very usual in reality, hence, it is necessary to investigate how the biased starting models can impact the inverted time-lapse models.

In Figure 18 and 19, the inverted time-lapse models from different strategies are plotted, and their model errors are plotted in Figure 20. We observe the PRS, SSPRS, CMS, and CDS fail to give a meaningful result, especially, the CMS and CDS are more sensitive to the biased starting models than others. Compared with other strategies, the DDS and SSCMS are more stable, the inverted results can still focus on the true reservoir change. But from the results of DDS and SSCMS, we note the obvious changes of reservoir position and the strong artifacts of negative velocity change near the reservoirs, which may mislead the reservoir interpretation.

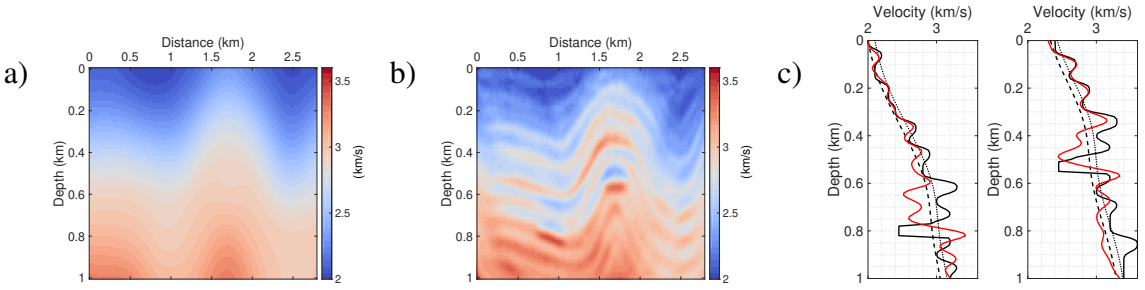

FIG. 16. (a) is the biased starting model which equals the unbiased model (Figure 3b) minus $100m/s$, and (b) the corresponding inverted baseline model. (c) are the traces abstracted at the distances 970m (left) and 1700m (right), and legends are the same as that in Figure 15.

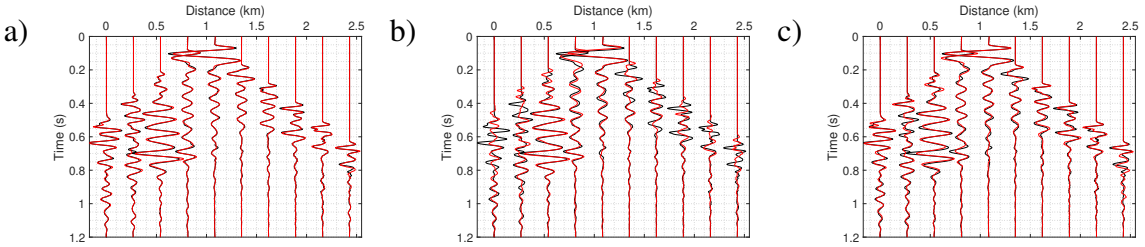

FIG. 17. Black curves are observed baseline data, and red curves are synthetic data of the inverted baseline models using (a) the unbiased starting model in Figure 3b, (b) the biased starting model in Figure 15a, and (c) the biased starting model in Figure 16a. All synthetic data can fit the observed data well.

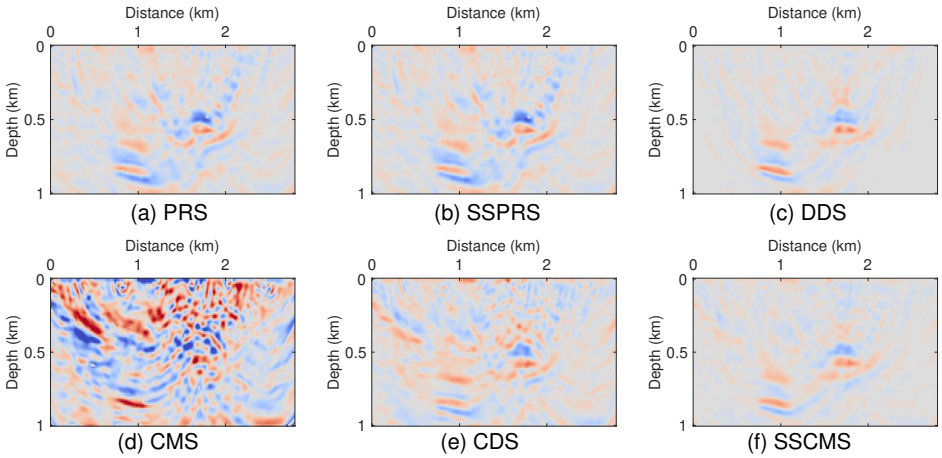

FIG. 18. Inverted time-lapse results of different strategies in the case of starting model (Figure 15a) is $100m/s$ larger than the unbiased one. All figures are clipped in the same color bar that in Figure 3b.

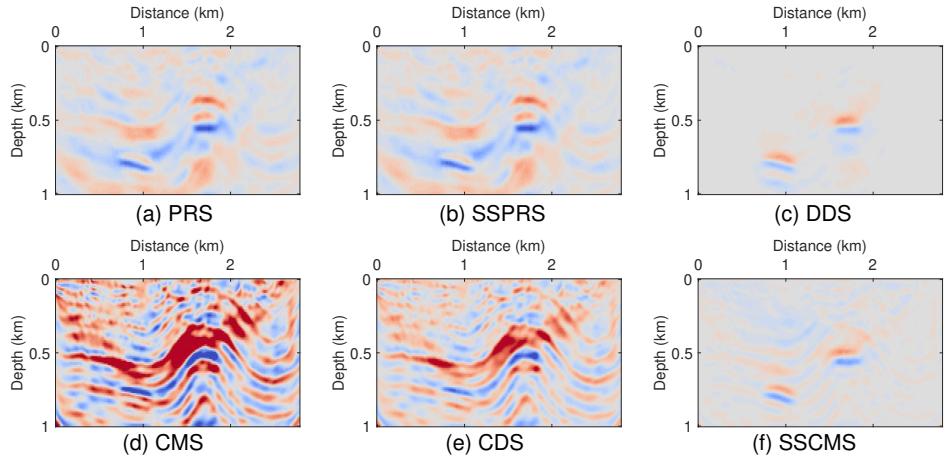

FIG. 19. Inverted time-lapse results of different strategies in the case of starting model (Figure 16a) is $100m/s$ smaller than the unbiased one. All figures are clipped in the same color bar that in Figure 3b.

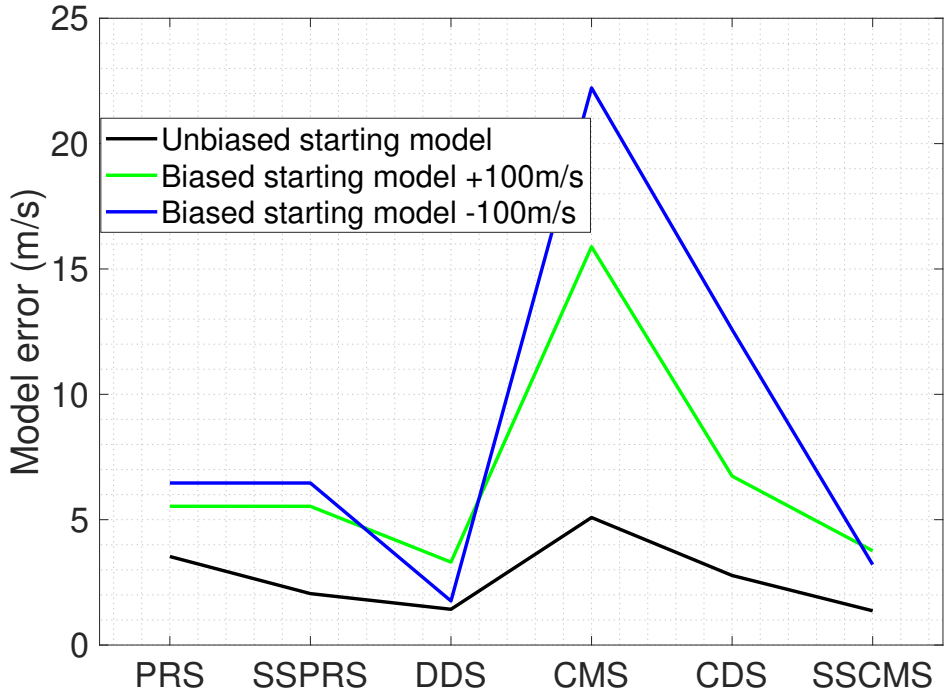

FIG. 20. Model errors of time-lapse models in Figure 5, 18 and 19.

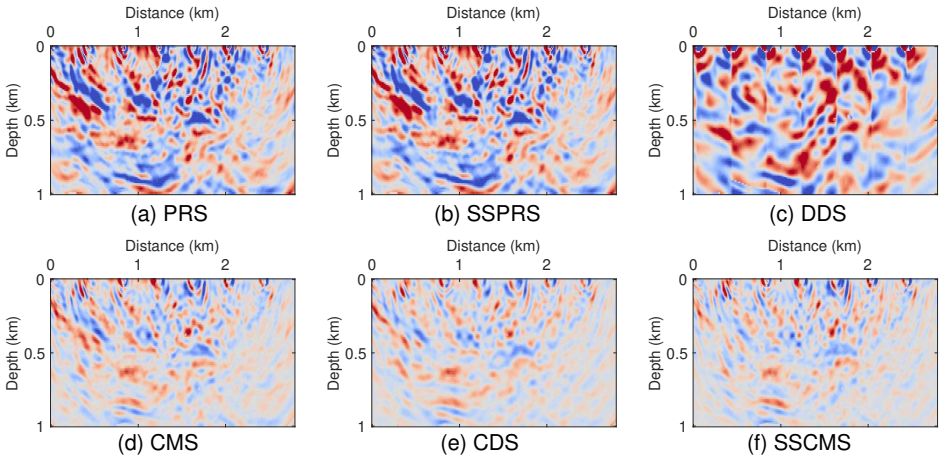

FIG. 21. Inverted time-lapse results of different strategies in the case of SNRs for both baseline and monitor data sets are 20, the monitor source locations are $10m$ larger than baseline source locations, and starting model (Figure 15a) is $100m/s$ larger than the unbiased one. All figures are clipped in the same color bar that in Figure 3b.

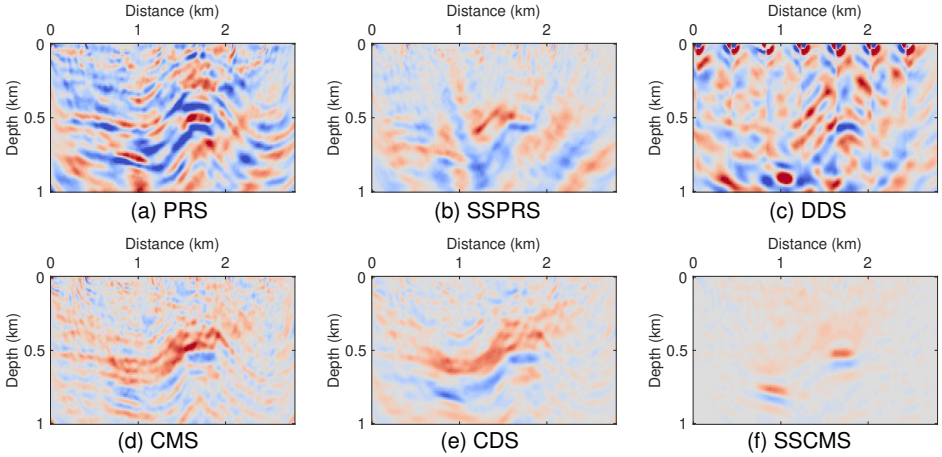

FIG. 22. Inverted time-lapse results of different strategies in the case of SNRs for both baseline and monitor data sets are 20, the monitor source locations are $10m$ larger than baseline source locations, and starting model (Figure 16a) is $100m/s$ smaller than the unbiased one. All figures are clipped in the same color bar that in Figure 3b.

Combined random noise, non-repeatable source locations, and biased starting models

In Figure 21 and 22, we test different strategies in the case of combining all conditions tested before. In the tests, SNRs for both baseline and monitor data sets are 20, the monitor source locations are $10m$ larger than baseline source locations, and biased starting models are employed (Figure 15a for Figure 21 and Figure 16a for Figure 22). And model errors of all results in Figure 21 and 22 are plotted in Figure 23. We observe only the SSCMS can survive under complex cases of combining different issues.

DISCUSSION AND CONCLUSIONS

From the results in this study, we observe:

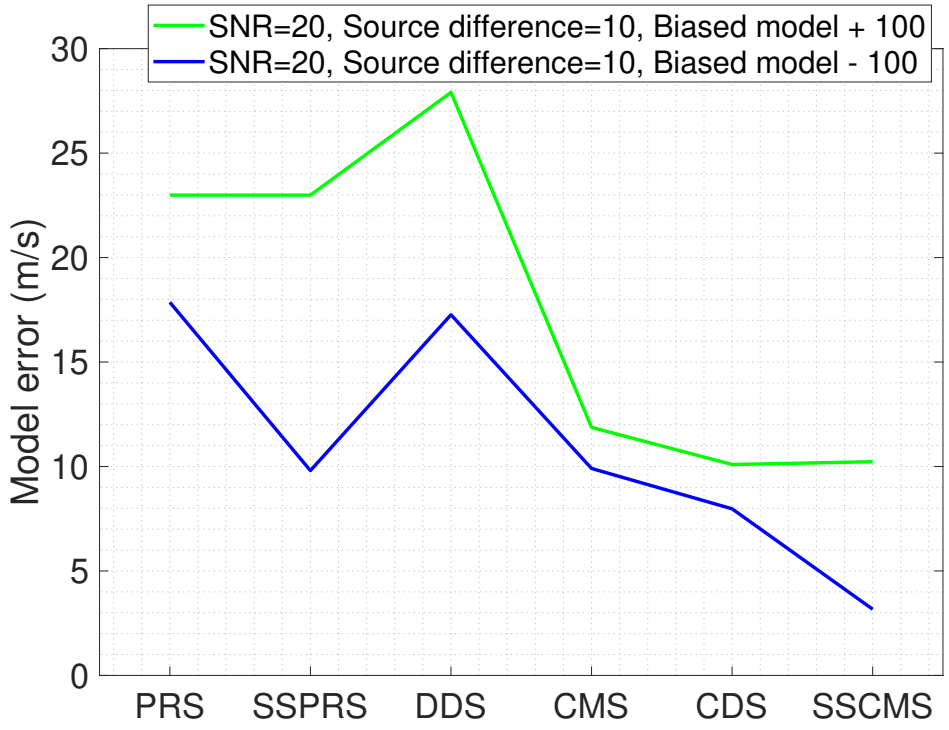

FIG. 23. Model errors of time-lapse results in Figure 21 and 22.

(1) The parallel strategy (PRS) has the artifacts caused by the difference of the convergences, is not noise resistant, and is sensitive to biased starting models.

(2) The double-difference strategy (DDS) is well applicable for the case of well-repeatable time-lapse surveys, but it is too sensitive to the difference in source locations

(3) The common-model strategy (CMS) cannot solve the artifacts resulting from the difference of the convergences, but can improve the anti-noise property, and is stable in unrepeatable source locations, but fails in the case of biased starting model.

(4) The central-difference strategy (CDS) has good performance in the cases of noisy data and non-repeatable source locations, also can decay the artifacts resulting from the difference of the convergences in some degree, but it fails in the case of biased starting model too.

(5) The stepsizes-sharing strategies can reduce artifacts caused by the convergences difference. Especially, the stepsize-sharing common-model strategy (SSCMS) has good performance on reducing the artifacts caused by the convergences difference, noisy data, non-repeatable source locations, and biased starting models. It may as a potential strategy for real field data inversion. The SSCMS can also save half of the time cost of seeking stepsizes when compared with the CMS and CDS.

(6) Biased starting models can lead to wrong reservoir positions and artifacts of negative reservoir changes rather than the correct positive ones. These may mislead the reservoir interpretation.

In this study, elastic effects are not taken into consideration, since we need to perform too many times FWI (110 times totally) which means it may take a too long time to implement elastic FWI. A better solution may be performing the acoustic FWI with elastic observed data (Zhou and Lumley, 2021a), but the remnant wavefields that cannot be mimicked by the acoustic wave equation may interfere with the comparisons between different strategies. Only the land model is discussed here, things could be different in the marine model, such as water level and/or velocity change. And the surface change is not considered either, which could happen between different seasons on the land and impact time-lapse inversion results. The subsurface change caused by the overburden pressure variation is all ignored in our study, it is often very small when compared with the reservoir change and could happen during the oil/gas production.

ACKNOWLEDGEMENTS

We thank the sponsors of CREWES for continued support. This work was funded by CREWES industrial sponsors and NSERC (Natural Science and Engineering Research Council of Canada) through the grant CRDPJ 543578-19. Partial funding also came from the Canada First Research Excellence Fund.

REFERENCES

Arts, R., Eiken, O., Chadwick, A., Zweigel, P., Van der Meer, L., and Zinszner, B., 2003, Monitoring of co2 injected at sleipner using time lapse seismic data, *in* Greenhouse Gas Control Technologies-6th International Conference, Elsevier, 347–352.

Asnaashari, A., Brossier, R., Garambois, S., Audebert, F., Thore, P., and Virieux, J., 2015, Time-lapse seismic imaging using regularized full-waveform inversion with a prior model: which strategy?: Geophysical prospecting, **63**, No. 1, 78–98.

Barkved, O., Buer, K., Halleland, K., Kjelstadli, R., Kleppan, T., and Kristiansen, T., 2003, 4d seismic response of primary production and waste injection at the valhall field, *in* 65th EAGE Conference & Exhibition, European Association of Geoscientists & Engineers, cp–6.

Barkved, O. I., Kristiansen, T., and Fjær, E., 2005, The 4d seismic response of a compacting reservoir—examples from the valhall field, norway, *in* SEG Technical Program Expanded Abstracts 2005, Society of Exploration Geophysicists, 2508–2511.

Bortoni, S., Barragan, S., Azevedo, G., Cypriano, L., Ferreira, A., Moreira, W., dos Reis, P., and Filho, W., 2021, Learnings from an fwi imaging study using 3d and 4d data over a postsalt field in campos basin, *in* First International Meeting for Applied Geoscience & Energy, Society of Exploration Geophysicists, 587–591.

Chadwick, R., Noy, D., Arts, R., and Eiken, O., 2009, Latest time-lapse seismic data from sleipner yield new insights into co2 plume development: Energy Procedia, **1**, No. 1, 2103–2110.

Fabien-Ouellet, G., Gloaguen, E., and Giroux, B., 2017, Time domain viscoelastic full waveform inversion: Geophysical Journal International, **209**, No. 3, 1718–1734.

Fu, X., and Innanen, K. A., 2021, An mcmc-based approach to time-lapse full-waveform inversion, *in* First International Meeting for Applied Geoscience & Energy, Society of Exploration Geophysicists, 3484–3489.

Fu, X., Romahn, S., and Innanen, K., 2020, Double-wavelet double-difference time-lapse waveform inversion, *in* SEG Technical Program Expanded Abstracts 2020, Society of Exploration Geophysicists, 3764–3767.

Greaves, R. J., and Fulp, T. J., 1987, Three-dimensional seismic monitoring of an enhanced oil recovery process: Geophysics, **52**, No. 9, 1175–1187.

Hicks, E., Hoeber, H., Houbiers, M., Lescoffit, S. P., Ratcliffe, A., and Vinje, V., 2016, Time-lapse full-waveform inversion as a reservoir-monitoring tool—a north sea case study: The Leading Edge, **35**, No. 10, 850–858.

Jack, I., 2017, 4d seismic—past, present, and future: The Leading Edge, **36**, No. 5, 386–392.

Kamei, R., Jang, U. G., Lumley, D., Takanashi, M., Nakatsukasa, M., Mouri, T., and Kato, A., 2017, Time-lapse full-waveform inversion for cross-well monitoring of microbubble injection, *in* 2017 SEG International Exposition and Annual Meeting, OnePetro.

Kazemeini, S. H., Juhlin, C., and Fomel, S., 2010, Monitoring co2 response on surface seismic data; a rock physics and seismic modeling feasibility study at the co2 sequestration site, ketzin, germany: Journal of Applied Geophysics, **71**, No. 4, 109–124.

Lailly, P., Bednar, J. et al., 1983, The seismic inverse problem as a sequence of before stack migrations: Conference on Inverse Scattering, Theory and Application, Society for Industrial and Applied Mathematics, Expanded Abstracts, 206–220.

Lumley, D. E., 2001, Time-lapse seismic reservoir monitoring: Geophysics, **66**, No. 1, 50–53.

Pevzner, R., Urosevic, M., Popik, D., Shulakova, V., Tertyshnikov, K., Caspari, E., Correa, J., Dance, T., Kepic, A., Glubokovskikh, S. et al., 2017, 4d surface seismic tracks small supercritical co2 injection into the subsurface: Co2crc otway project: International Journal of Greenhouse Gas Control, **63**, 150–157.

Raknes, E. B., and Arntsen, B., 2014, Time-lapse full-waveform inversion of limited-offset seismic data using a local migration regularization: Geophysics, **79**, No. 3, WA117–WA128.

Raknes, E. B., Weibull, W., and Arntsen, B., 2013, Time-lapse full waveform inversion: Synthetic and real data examples, *in* 2013 SEG Annual Meeting, OnePetro.

Ross, C. P., and Altan, M. S., 1997, Time-lapse seismic monitoring: Some shortcomings in nonuniform processing: The Leading Edge, **16**, No. 6, 931–937.

Routh, P., Palacharla, G., Chikichev, I., and Lazaratos, S., 2012, Full wavefield inversion of time-lapse data for improved imaging and reservoir characterization, *in* SEG Technical Program Expanded Abstracts 2012, Society of Exploration Geophysicists, 1–6.

Shin, C., Jang, S., and Min, D.-J., 2001, Improved amplitude preservation for prestack depth migration by inverse scattering theory: Geophysical prospecting, **49**, No. 5, 592–606.

Tarantola, A., 1984, Inversion of seismic reflection data in the acoustic approximation: Geophysics, **49**, No. 8, 1259–1266.

Virieux, J., and Operto, S., 2009, An overview of full-waveform inversion in exploration geophysics: Geophysics, **74**, No. 6, WCC1–WCC26.

Wang, Z., Cates, M. E., and Langan, R. T., 1998, Seismic monitoring of a co2 flood in a carbonate reservoir: A rock physics study: Geophysics, **63**, No. 5, 1604–1617.

Yang, D., Liu, F., Morton, S., Malcolm, A., and Fehler, M., 2016, Time-lapse full-waveform inversion with ocean-bottom-cable data: Application on valhall field: Geophysics, **81**, No. 4, R225–R235.

Yang, D., Meadows, M., Inderwiesen, P., Landa, J., Malcolm, A., and Fehler, M., 2015, Double-difference waveform inversion: Feasibility and robustness study with pressure data: Geophysics, **80**, No. 6, M129–M141.

Zhang, Z., and Huang, L., 2013, Double-difference elastic-waveform inversion with prior information for time-lapse monitoring: Geophysics, **78**, No. 6, R259–R273.

Zheng, Y., Barton, P., and Singh, S., 2011, Strategies for elastic full waveform inversion of time-lapse ocean bottom cable (obc) seismic data, *in* SEG Technical Program Expanded Abstracts 2011, Society of Exploration Geophysicists, 4195–4200.

Zhou, W., and Lumley, D., 2021a, Central-difference time-lapse 4d seismic full-waveform inversion: Geophysics, **86**, No. 2, R161–R172.

Zhou, W., and Lumley, D., 2021b, Non-repeatability effects on time-lapse 4d seismic full waveform inversion for ocean-bottom node data: Geophysics, **86**, No. 4, 1–60.